Journal of Geophysical Research: Space Physics

RESEARCH ARTICLE
10.1029/2018JA025473

Characteristics of Subpacket Structures in Ground EMIC Wave Observations

Bharati Kakad[1,2], Yoshiharu Omura[2], Amar Kakad[1], Aditi Upadhyay[1], and Ashwini K. Sinha[1]

[1]Indian Institute of Geomagnetism, Navi Mumbai, India, [2]Research Institute for Sustainable Humanosphere, Kyoto University, Kyoto, Japan

Key Points:
- Amplitude-frequency dependence of EMIC subpacket structures is unaltered during their propagation to the ground
- EMIC waves observed on the ground are mainly (>70%) associated with right-handed elliptical polarization
- Duration of subpacket structure is found to be proportional to its maximum amplitude

Correspondence to:
B. Kakad,
bkakad9@gmail.com

Citation:
Kakad, B., Omura, Y., Kakad, A., Upadhyay, A., & Sinha, A. K. (2018). Characteristics of subpacket structures in ground EMIC wave observations. *Journal of Geophysical Research: Space Physics*, *123*, 8358–8376. https://doi.org/10.1029/2018JA025473

Received 14 MAR 2018
Accepted 28 SEP 2018
Accepted article online 3 OCT 2018
Published online 27 OCT 2018

Abstract Recent studies using satellite observations have reported that subpacket structures play an important role in determining the characteristics of electromagnetic ion cyclotron (EMIC) rising/falling tone emissions. The purpose of the present study is to investigate the subpacket structure characteristics in the ground observations of the EMIC waves. It will help us understand the effect of propagation on the EMIC subpacket structures. The induction coil magnetometer observations from Maitri, Antarctica (Geog. 70.77°S, 11.75°E, Geomag. 63.11°S, 53.59°E, $L = 5$), are used. Six quiet time EMIC events during 2015–2016 are analyzed and their details are presented. Based on their frequency extent in the power spectrum, four (two) events are speculated to be linked with proton (helium) band EMIC waves. For these events, the EMIC rising tone occurrence periods are estimated to be 1.9–6.7 min. Our analysis suggests that the amplitude-frequency dependence of EMIC subpacket structures is less significantly affected during their prorogation to the ground. Overall, it is found that more than 70% of the time the EMIC waves are right-handed elliptical polarized. An interesting feature is that the duration of the subpacket structure is found to be directly proportional to the EMIC wave amplitude. The observed characteristics and tendencies followed by EMIC subpacket structures on the ground are examined in the light of existing nonlinear wave theory and they are in good agreement. The EMIC wave amplitudes on the ground are found to be 16–80 times lower than the expected theoretical estimates of the wave amplitudes in the source region.

1. Introduction

Electromagnetic ion cyclotron (EMIC) waves with ultralow frequency (0.1–5 Hz) range are observed by various spacecrafts in Earth's magnetosphere (Fraser et al., 2010; Meredith et al., 2014; Nakamura et al., 2016; Park et al., 2016; Pickett et al., 2010; Remya et al., 2015; Wang et al., 2015). These waves play an important role in the dynamics of the Earth's radiation belts by contributing to loss mechanism of relativistic electrons through a process called anomalous cyclotron resonance (Jordanova et al., 2008; Lorentzen et al., 2000; Meredith et al., 2003; Summers & Thorne, 2003; Summers et al., 2007). EMIC waves consist of several closely placed discrete rising tone structures widely known as EMIC triggered emissions (Omura et al., 2010; Pickett et al., 2010). These EMIC rising tone emissions can efficiently scatter the relativistic electrons into the loss cone, resulting significant loss of relativistic electrons from the radiation belt (Carson et al., 2013; Kubota et al., 2015; Millan & Thorne, 2007; Omura & Zhao, 2013; Rodger et al., 2008). Some recent studies have shown that combined scattering by EMIC waves and chorus waves can considerably decrease the lifetimes of electrons having energies greater than 1–2 MeV over the whole range of equatorial pitch-angles, which explains some of the rapid electron flux dropouts observed in the outer radiation belt (Mourenas et al., 2016; Zhang et al., 2017). EMIC waves are generated by the ion cyclotron instability of energetic ions with an anisotropic energy distribution ($T_\perp > T_\parallel$) in the Earth's equatorial region of magnetosphere (Gendrin et al., 1984; Gomberoff & Neira, 1983; Young et al., 1981). In recent years, many interesting studies of EMIC waves have been carried out using both satellite and ground observations (K.-H. Kim et al., 2017; Min et al., 2012; Park et al., 2017; Usanova et al., 2010, 2014). These EMIC rising tone emissions are generally observed in different bands, for example, proton (H^+), helium (He^+), and oxygen (O^+) depending on the ambient parameters in the generation region (Saikin et al., 2015; Yu et al., 2015).

Earlier it was believed that each EMIC rising tone is a single emission with monotonically increasing frequency. However, recently, Nakamura et al. (2015) reported the presence of subpacket structures in the EMIC rising

©2018. American Geophysical Union. All Rights Reserved.

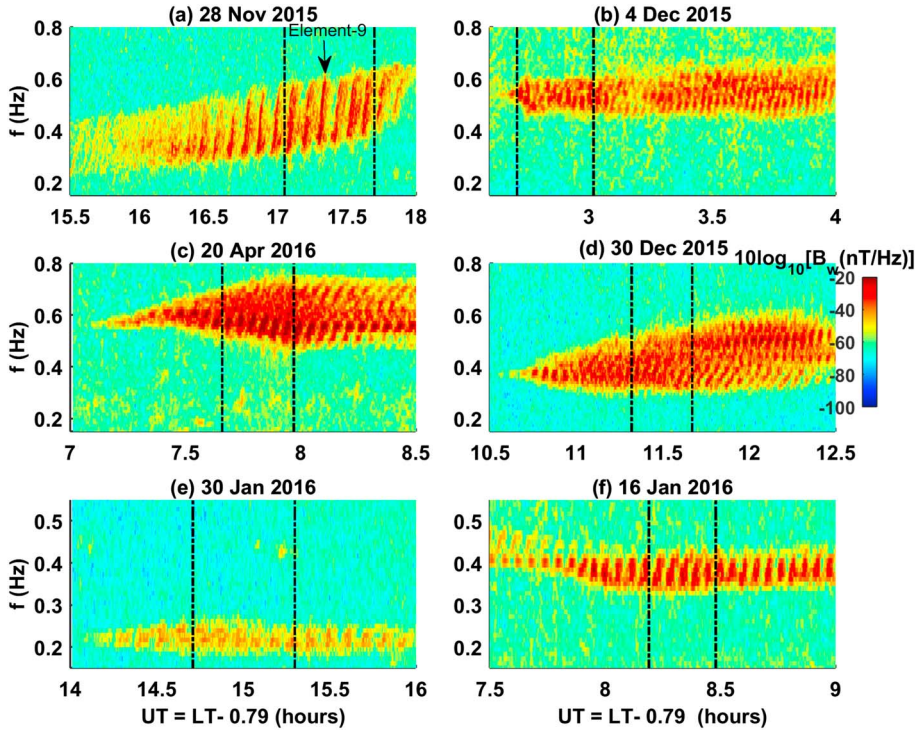

Figure 1. The Fourier spectrogram for 28 November 2015, 4 December 2015, 20 April 2016, 30 December 2015, 30 January 2016, and 16 January 2016 are plotted in the panels (a) to (f), respectively. The presence of strong and distinct electromagnetic ion cyclotron rising tone emissions are clearly seen on these days. The vertical dotted lines represent the time interval taken for the analysis of instantaneous amplitude-frequency.

tone emissions observed by the THEMIS spacecraft. Their study suggests that the single EMIC rising tone emission consist of several smaller structures called as subpackets. The hybrid simulations demonstrated that the EMIC triggered emission is formed as a train of subpackets generated at different rising frequencies (Shoji & Omura, 2013). Such subpacket structures are also evident in the satellite observations of whistlers mode chorus waves (Santolík et al., 2014). It is believed that the nonlinear wave growth process inherently controls the formation of subpacket structures and their characteristics. Thus, detailed analyses of characteristics of these subpacket structures are needed for better understanding of the generation of EMIC rising tone and their role in the energetic particle loss processes.

In this paper, we have studied the subpacket structures in the EMIC waves observed on the ground. We have chosen six magnetically quiet time EMIC events recorded at the Indian Antarctic station, Maitri (geographic coordinates: 70.7°S, 11.8°E; geomagnetic coordinates: 63.1°S, 53.6°E), by the induction coil magnetometer (ICM). This paper is organized as follows; EMIC wave observations and data analysis techniques are described in section 2. General characteristics of EMIC waves and polarization analysis are given in sections 3 and 4, respectively. An instantaneous amplitude-frequency investigation of EMIC waves is elaborated in section 5. The EMIC wave observations are compared with nonlinear wave theory in section 6. Finally, the present work is summarized and concluded in section 7.

2. Observations and Data Analysis

We used magnetic field data recorded by the ICM at Indian Antarctic station Maitri ($L = 5$). The location of Maitri is unique as it lies outside (within) the auroral oval during geomagnetically quiet (disturbed) time periods. The ICM (LEMI-30i provided by Lviv Centre of Institute for Space Research, Ukraine) composes of three induction coils, which are aligned in the geographic north-south ($+x$ is north) and geographic east-west ($+y$ is east) directions and the third induction coil is placed in the vertical direction ($+z$ is downward). The ICM measures variations in the magnetic field at higher sampling rates than any other traditionally employed magnetometers. In the present study, we have analyzed six EMIC November 2015 to April 2016. These 6 days, namely, 28 November 2015, 4 December 2015, 20 April 2016, 30 December 2015, 30 January 2016, and 16 January 2016 are magnetically quiet days ($Ap = 2 - 6$). Hereafter, we call them as events 1–6, respectively. The

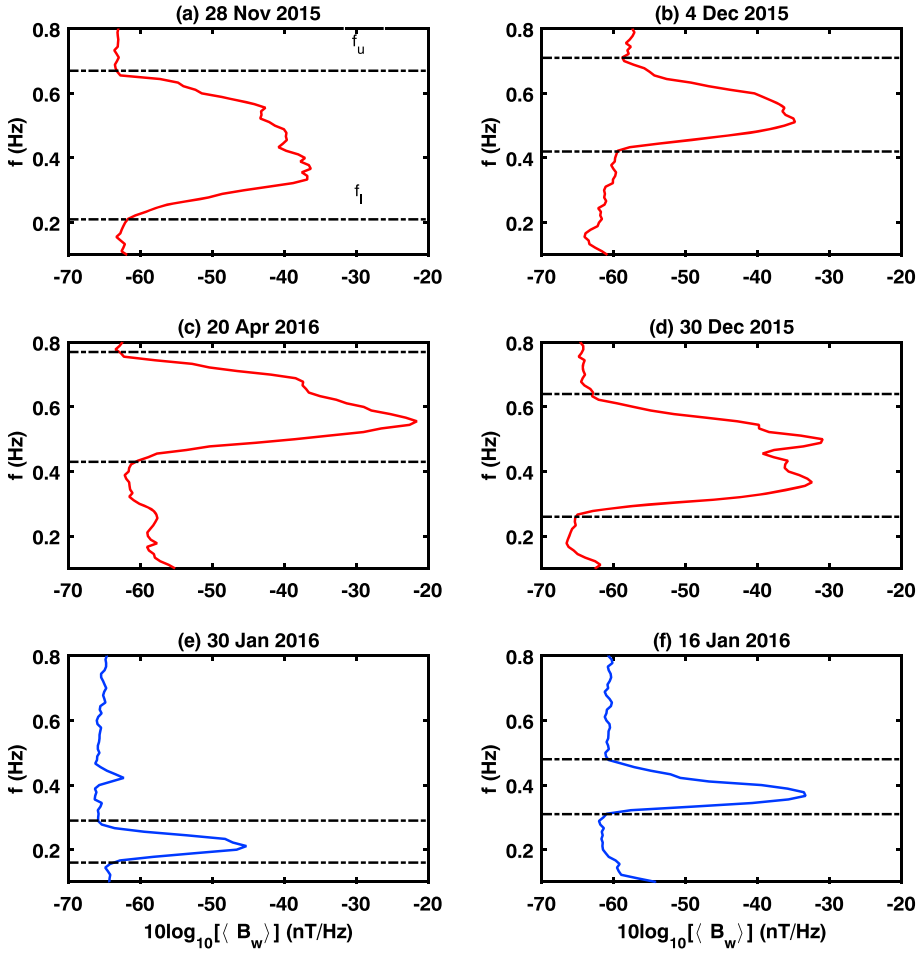

Figure 2. Panels (a)-(f) shows the frequency as a function of the average power spectral densities over a time window bounded by start time (t_s) and end time (t_e) of the electromagnetic ion cyclotron wave activity ($\langle B_w \rangle_{t_s}^{t_e}$) for events 1–6 respectively. The lower and upper horizontal dotted lines indicate the lower (f_l) and upper (f_u) frequency bounds for the electromagnetic ion cyclotron wave activity.

magnetic field variations recorded by three coils at time t are termed as B_{wx}^t, B_{wy}^t, and B_{wz}^t. The sampling rate of the data is 256 Hz. For each component, the Fourier spectrogram is obtained by taking a window of 90 s with an overlap of 95%. Thus, the spectrogram has a resolution of 0.011 Hz in frequency domain and 4.5 s in time domain. The power spectral densities of these three components (i.e., $P_{wx}^{f,t}$, $P_{wy}^{f,t}$, and $P_{wz}^{f,t}$) are used to obtain the Fourier spectrogram of total variation in magnetic field such that $P_w^{f,t} = \sqrt{|P_{wx}^{f,t}|^2 + |P_{wy}^{f,t}|^2 + |P_{wz}^{f,t}|^2} = B_w^{f,t}$. We examined the Fourier spectrograms of all 6 days to identify the EMIC wave activities.

The other lower frequency pulsation phenomenon is Intervals of Pulsations with Diminishing Periods (IPDPs; Pikkarainen et al., 1983). In general, IPDPs are frequency modulated pulsations occurring in the range of Pc1–Pc2 and it shows a peculiar feature in the spectrogram. For a typical IPDP event, a frequency increase from fraction of Hertz to 1 Hz within half an hour is observed (Kangas et al., 1998). These IPDP pulsations stand out prominently against any other waves because of their well-defined large frequency modulation (Clilverd et al., 2015; Yahnina et al., 2003). It is a manifestation of the particle injection into the Earth's magnetosphere from the tail-side. These IPDPs are mostly observed around the evening sector. A short duration prominent frequency modulation linked with IPDP can be used as a tool to identify it in the frequency spectrogram of the EMIC waves. The discrete rising tone emissions are clearly seen in the EMIC wave events 1–6 studied here, and they do not show any features of IPDP-type pulsations (see Figures 1a–1f).

Table 1
General Characteristics of EMIC Waves

Event no.	Day	f_l (Hz)	f_u (Hz)	f_c (Hz)	Start time, t_s UT (hr)	End time, t_e UT (hr)	Periodicity (min)	Possible EMIC band	AE_{max} (nT)
1	28 Nov 2015	0.21	0.66	0.38	15.5	18	6.69	H-band	125
2	4 Dec 2015	0.42	0.71	0.52	2.5	4	1.94	H-band	49
3	20 Apr 2016	0.43	0.79	0.56	7.1	8.5	3.2	H-band	289
4	30 Dec 2015	0.26	0.64	0.44	10.5	12.5	2.99	H-band	84
5	30 Jan 2016	0.16	0.29	0.22	14	16	6.67	He-band	116
6	16 Jan 2016	0.31	0.48	0.38	7.5	9.5	3.27	He-band	86

Note. The lower, upper, and centered frequency bounds; start and end time; and periodicities associated with all six EMIC events 1–6. The speculated EMIC bands are also mentioned in the second last column. EMIC = electromagnetic ion cyclotron.

3. General Characteristics of EMIC Waves

In this section, we discuss the general characteristics of EMIC waves observed on the 6 days chosen in the present study. The Fourier spectrograms for 28 November 2015, 4 December 2015, 20 April 2016, 30 December 2015, 30 January 2016, and 16 January 2016 are plotted in Figures 1a–1f, respectively. The presence of strong and distinct EMIC rising tone emissions are clearly seen on these days. The vertical dotted lines represent the time interval taken for the analysis of instantaneous amplitude-frequency in section 5. Strong EMIC wave activities are clearly evident in the frequency range of 0.2–0.8 Hz for all events. In order to obtain the lower and upper frequency limits of EMIC wave activity, we estimated the average power spectral densities over a time window bounded by a start time (t_s) and an end time (t_e) of the EMIC wave activity. The EMIC wave frequency for events 1–6 are plotted as a function of the average wave power spectral densities, $\langle B_w \rangle_{t_s}^{t_e}$, Figures 2a–2f respectively. The lower and upper horizontal dotted lines marked in Figures 2a–2f indicate the lower (f_l) and upper (f_u) frequency bounds in which the EMIC wave activity is confined. The EMIC waves show a maximum power at the centered frequency f_c. The start and end times, lower, upper, and centered frequencies for events 1–6 are given in Table 1.

It may be noted that the distinct EMIC rising tone emissions are observed on these days, but the occurrence frequency of these rising tone emissions (i.e., EMIC wave repetitive period) is different for different days. For events 2, 4, and 6, the EMIC rising tone emissions are closely placed as compared to events 1, 3, and 5. In order to examine the periodicities associated with the EMIC rising tone emission, we estimated the averaged spectrogram power from frequency f_1 to f_2. In this way, we obtain the time variation of averaged spectrogram power, $\langle B_w \rangle_{f_1}^{f_2}$, associated with the average frequency, $\langle f \rangle = (f_1 + f_2)/2$, which are shown in Figures 3a–3f for events 1–6, respectively. Here frequencies f_1 and f_2 are chosen such that they are close to the centered frequency f_c. For these events, each peak seen in the time variation of $\langle B_w \rangle_{f_1}^{f_2}$ indicate the EMIC rising tone emission (see left panels of Figure 3). This time varying signal of averaged spectrogram power is subjected to Fourier transform to estimate the dominant periods present in the EMIC wave activity. These power spectrums are shown in Figures 3g–3l, respectively. The dominant periods are manifested in the power spectrums shown in the right-side panels of Figure 3. We find that the dominant periods associated with the EMIC wave activity are 1.94–6.69 min and these estimated periods are given in Table 1. It suggests that the EMIC rising tone emissions occur at a time interval of 1.94–6.69 min for events 1–6.

The short repetition periods of EMIC waves observed in the present study fall under the ULF frequency range. The presence of such repetitive periods in EMIC waves have been reported earlier using both ground-based instruments and satellite experiments (Loto'Aniu et al., 2009; Mursula et al., 2001; Rasinkangas & Mursula, 1998) and they are attributed to the EMIC wave modulation by Pc4 (15–150 s) and Pc5 (150–600 s) pulsations. On the other hand, another study by Usanova et al. (2010) using simultaneous satellite and ground observations suggests that these repetitive structures of the EMIC waves observed on the ground cannot be explained by the ULF wave. They have found that the EMIC wave repetition period on the ground can be approximated by the field aligned Alfvenic travel time. Although observationally we know about the modulation of Pc1 EMIC waves by Pc4/Pc5 ULF waves, the physical mechanism responsible for such modulation is not well understood (Menk, 2011). Here we suggest the Pc5 ULF waves associated with magnetic field line oscillations as a possible source for the modulation of EMIC waves. Nonlinear theory suggests that the triggering of EMIC waves needs a constant frequency ion cyclotron wave with appropriate amplitude termed as

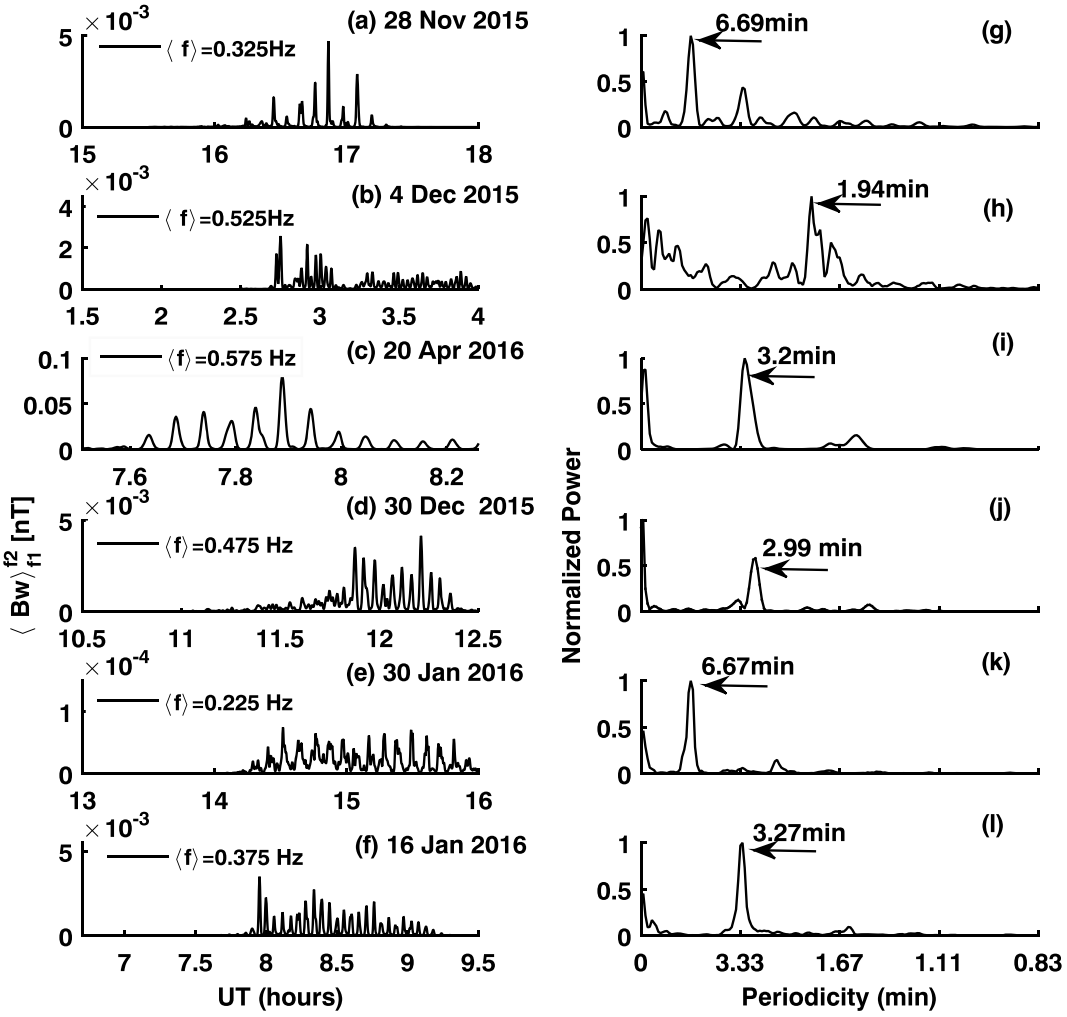

Figure 3. Time variations of averaged spectrogram power, $\langle B_w \rangle_{f_1}^{f_2}$, associated with the average frequency, $\langle f \rangle = (f_1 + f_2)/2$, are shown for events 1–6, respectively, in panels (a)–(f). Here frequencies f_1 and f_2 are chosen such that they are close to the centered frequency f_c. Each peak seen in the time variation of $\langle B_w \rangle_{f_1}^{f_2}$ indicates the electromagnetic ion cyclotron rising tone emission. Their corresponding power spectrums are shown in right-side panels (g)–(i). The dominant periods are found to be 1.9–6.7 min.

the threshold amplitude B_{th} (Omura et al., 2010). The theoretical estimate of the threshold wave amplitude required for the nonlinear wave growth is affected by the parameter a (refer equation (7) in section 6). It may be noted that this threshold wave amplitude becomes smaller when the magnetic field gradient becomes smaller. The field line oscillations can alter the magnetic field gradient ($\partial\Omega_H/\partial h$) and the parameter a, which plays an important role in controlling the threshold amplitude (B_{th}) required for the growth of EMIC wave.

The identification of EMIC bands in the satellite data is relatively easy, as one has the information about the local proton gyrofrequency. Generally, EMIC waves generated in the equatorial latitudes and then propagate along the magnetic field lines to the high latitude ionosphere. Their interaction with the anisotropic ionospheric plasma results in the compressional mode. A part of EMIC wave energy can get trapped into the F-region ionospheric duct. This causes the wave to propagate horizontally to lower or higher latitudes. Whereas some of EMIC wave energy can penetrate to the atmosphere, while propagating along magnetic field lines (Johnson & Cheng, 1999; E.-H. Kim & Johnson, 2016). Thus, identifying bands from the ground observations of EMIC wave is not straightforward. Simulation studies of EMIC waves have demonstrated that the frequency extent of proton band is larger than the helium band (Shoji et al., 2011). A careful scrutiny of spectrograms indicates that for events 1–4 the frequency extent $\Delta f = f_u - f_l$ is in the range of 0.3–0.45 Hz, whereas for events 5 and 6 it is in the range of 0.13–0.17 Hz. As the frequency extent is considerably smaller for events

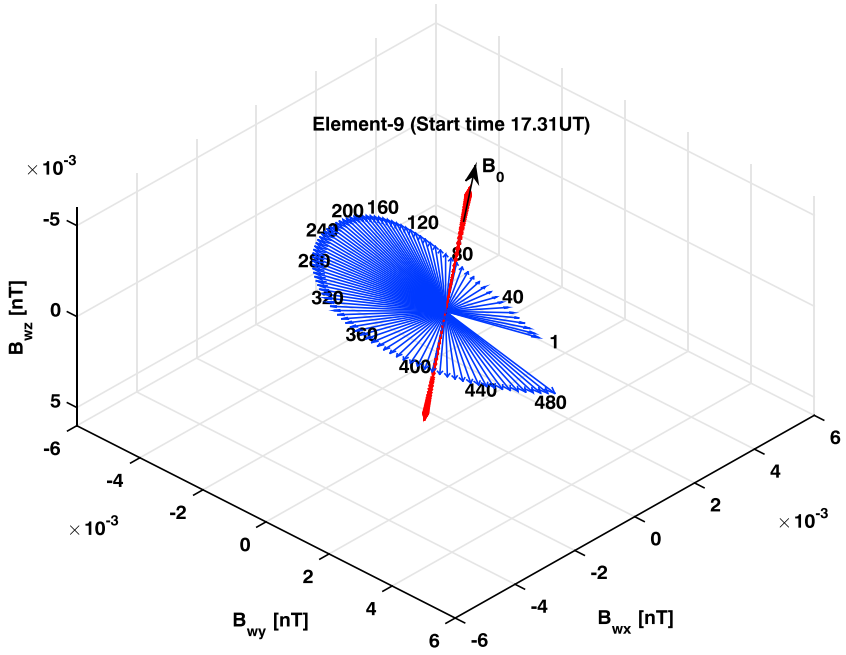

Figure 4. Time evolution of $\vec{B}_{w\perp}$ (blue color) and $\vec{B}_{w\|}$ (red color) over 1.875 s for electromagnetic ion cyclotron rising tone emission observed on 28 November 2015 starting at 17.31 UT (i.e., element-9) is shown. Each arrow representing $\vec{B}_{w\perp}$ is plotted at every 5/256 s and they are marked with the text at every 40/256 s. The direction of increase of time stamping (i.e., from 1 to 480) indicates the direction of rotation of perpendicular wave vector.

5 and 6, we speculate that EMIC wave activity seen on those days might be associated with helium band. On the other hand, events 1–4 could be associated with proton band EMIC waves. Thus, we propose that events 1–4 and events 5–6 could possibly be associated with the proton and helium band EMIC waves, respectively.

4. Polarization and Eccentricity

In this section, we have examined the polarization characteristics of the EMIC waves. Let us assume that B is the ambient magnetic field at Maitri. Using the International Geomagnetic Reference Field (IGRF) model we got $B = [B_x = 16190, B_y = -8919, B_z = -34403]$, where the magnetic field components are expressed in the units of nT. For each event, the magnetic field variations recorded by ICM were filtered using Butterworth bandpass filter of order three for the duration of EMIC wave activity. The lower and higher frequency cutoffs were chosen as f_l and f_u while applying a bandpass filter to the raw data. These filtered ICM signals are denoted by $\vec{B}_w = [B_{wx}, B_{wy}, B_{wz}]$ and used in the further analysis. Let us assume that the wave makes an angle of θ with the ambient magnetic field vector $\vec{B}$. First, we estimated the wave vector parallel ($\vec{B}_{w\|}$) and perpendicular ($\vec{B}_{w\perp}$) to the ambient magnetic field by using the following two equations.

$$\vec{B}_{w\|} = \left[\frac{\vec{B}_w \cdot \vec{B}}{|\vec{B}|}\right]\frac{\vec{B}}{|\vec{B}|}, \tag{1}$$

$$\vec{B}_{w\perp} = \vec{B}_w - \vec{B}_{w\|} \tag{2}$$

The clockwise (anticlockwise) rotation of perpendicular wave vector $\vec{B}_{w\perp}$ in the plane perpendicular to the direction of $\vec{B}$ represents the right (left) handed polarization of wave. As an example, in Figure 4, we have shown the time evolution of $\vec{B}_{w\perp}$ (blue color) and $\vec{B}_{w\|}$ (red color) over 1.875 s for the EMIC rising tone emission observed on 28 November 2015 starting at 17.31 UT (i.e., element-9). Each arrow representing $\vec{B}_{w\perp}$ is plotted at every 5/256 s and they are marked with the text at every 40/256 s. The direction in which these time stamping is increasing (i.e., from 1 to 480) indicates the direction of rotation of the perpendicular wave vector. It is evident from this analysis that the EMIC wave is right-handed polarized during this time interval.

Now we calculate the polarization for all EMIC events. Over one wave period T, vector $\vec{B}_{w\perp}$ will roughly complete one rotation in the perpendicular plane. To find the sense of rotation of $\vec{B}_{w\perp}$, we estimated a cross

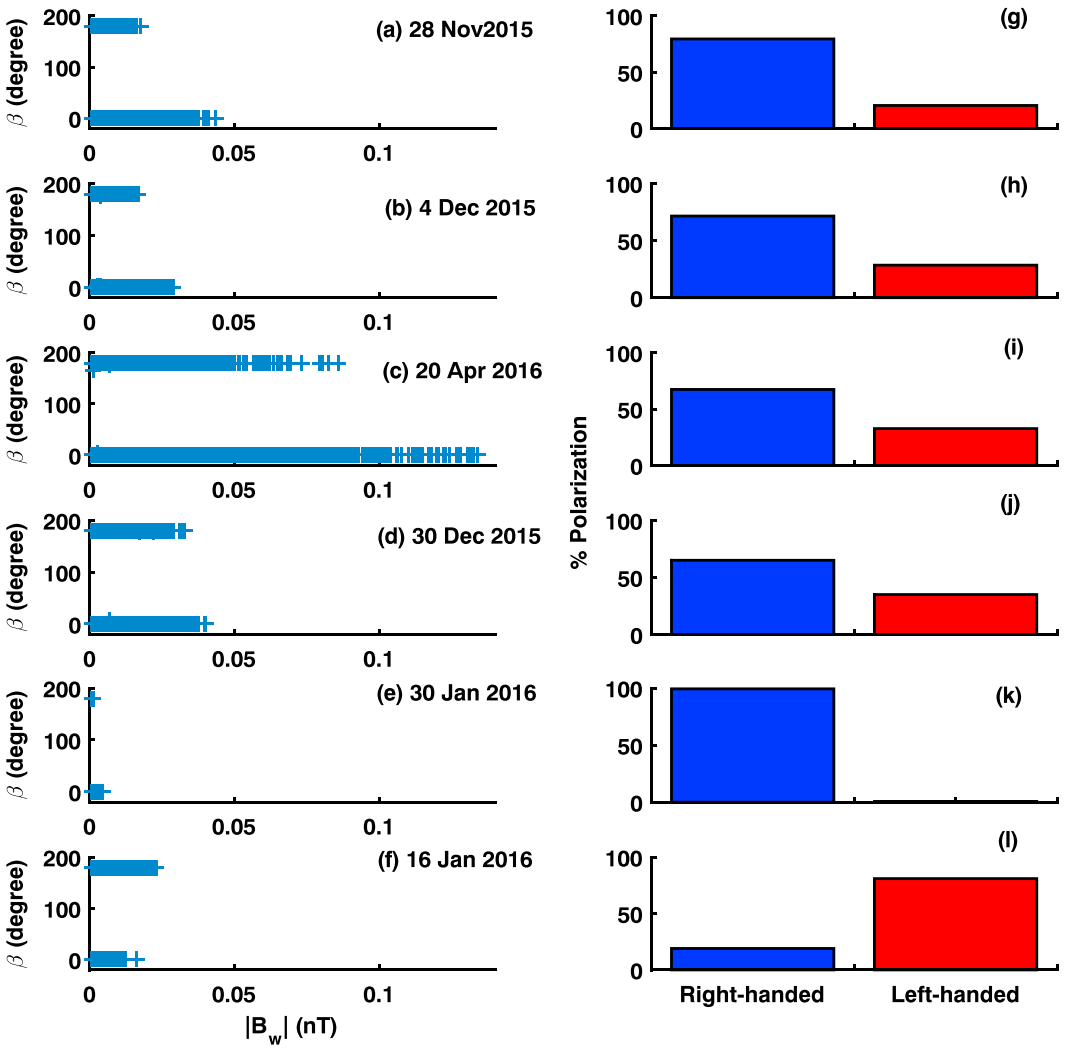

Figure 5. (a)–(f) Plot of β as a function of wave amplitude is shown for events 1–6. When β is zero (180°) then the wave has right-handed (left-handed) polarization. (g)–(l) The percentage occurrence of right-handed and left-handed polarization for these events is shown here.

product of $\vec{B}^{t}_{w\perp}$ and $\vec{B}^{t+T/4}_{w\perp}$. The resultant vector, $\vec{R} = \vec{B}^{t}_{w\perp} \times \vec{B}^{t+T/4}_{w\perp}$, will point in the direction perpendicular to the plane containing $\vec{B}_{w\perp}$. Further, we estimated angle β using the following equation,

$$\beta = \cos^{-1}\left[\left(\frac{\vec{B}}{|\vec{B}|}\right)\cdot\left(\frac{\vec{R}}{|\vec{R}|}\right)\right]. \tag{3}$$

Here β is the angle between $\vec{B}$ and $\vec{R}$, and it can have two values, that is, either zero or 180°. When β is zero (180°), $\vec{R}$ is pointing in the direction (opposite direction) of $\vec{B}$ and then the wave has right-handed (left-handed) polarization. Thus, we estimated β at an interval of $T/4$ for the duration of EMIC wave activity. The value of T is taken as $1/f_c$. While computing β, additional condition of $|\vec{B}_{w\perp}|, |\vec{B}_{w\|}| > 5\times10^{-4}$ nT is applied, so that the polarization associated with EMIC wave with sufficient strength (well above noise level) is taken into account. The plot of β as a function of wave amplitude is shown in Figures 5a–5f for the events 1–6, respectively. The percentage occurrence of right-handed and left-handed polarization for these events are shown in Figures 5g–5l. We find that more than 70% of times the EMIC events 1–5 are associated with the right-handed polarization. Whereas for event 6, mainly the left-handed polarization is seen. It is known that EMIC waves have left-handed polarization in the generation region and during their propagation to high latitudes along magnetic field lines it gets changed to right-handed polarization (Johnson & Cheng, 1999; H. Kim et al., 2010). Hence, our

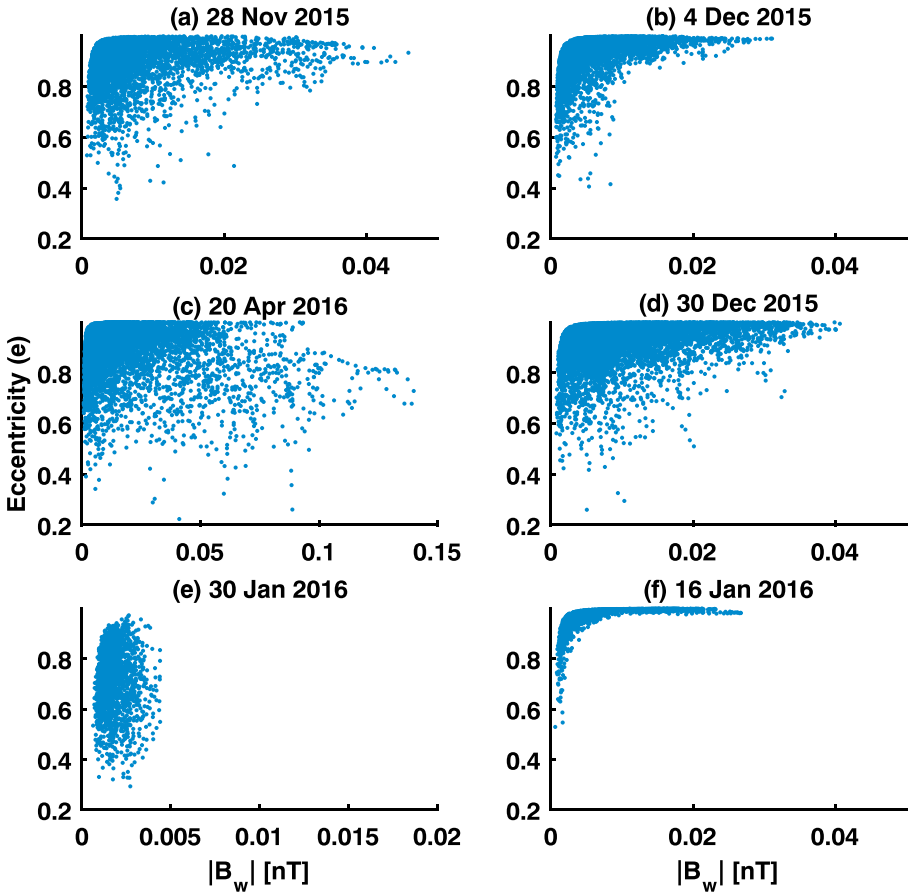

Figure 6. (a)-(f) Eccentricity is shown as a function of wave magnitude $|B_w|$ for all events. We found that eccentricity dominantly lies in the range of $0.5 \leq e < 1$. It suggests that electromagnetic ion cyclotron waves observed on the ground are mostly characterized by elliptical polarization.

results are in general agreement with the earlier studies. However, it is seen that the EMIC waves sometime do propagate to the ground without change in their polarization as seen in event 6.

We have also looked into eccentricity of the elliptical trajectory made by the movement of perpendicular wave vector $\vec{B}_{w\perp}$. Eccentricity is defined as $\sqrt{1 - b^2/a^2}$ where a and b are the lengths of semimajor and semiminor axes of the ellipse, respectively. We identified the minimum and maximum magnitude of $\vec{B}_{w\perp}$ during half wave period ($T/2$) and treated it as the semiminor and semimajor axes of ellipse of polarization. So the eccentricity can be computed using the following equation,

$$e = \sqrt{1 - \frac{\left[|\vec{B}_{w\perp}|_{min}\right]^2}{\left[|\vec{B}_{w\perp}|_{max}\right]^2}}. \tag{4}$$

We have computed eccentricity only if the conditions $|\vec{B}_{w\perp}|, |\vec{B}_{w\parallel}| > 5 \times 10^{-4}$ nT are satisfied. This assures that the estimated eccentricity values are associated with the sufficiently stronger EMIC wave signal (above noise level). In Figures 6a–6f, eccentricity is shown as a function of wave magnitude $|B_w|$ for all events. We found that eccentricity dominantly lies in the range of $0.5 \leq e < 1$ for more than 99% of times for all events except for event 5 (30 January 2016), for which 5% of times the eccentricity was found to be in the range of $0 < e < 0.5$. Thus, this exercise suggest that the EMIC waves observed on ground are characterized by right-handed elliptical polarization. Occasionally, left-handed elliptical polarization is also found to be present.

5. Instantaneous Amplitude-Frequency Relation

In this section, we describe the calculations of instantaneous amplitude and frequency of the EMIC waves and identification of subpacket structures. To demonstrate this analysis, we consider an example of a single

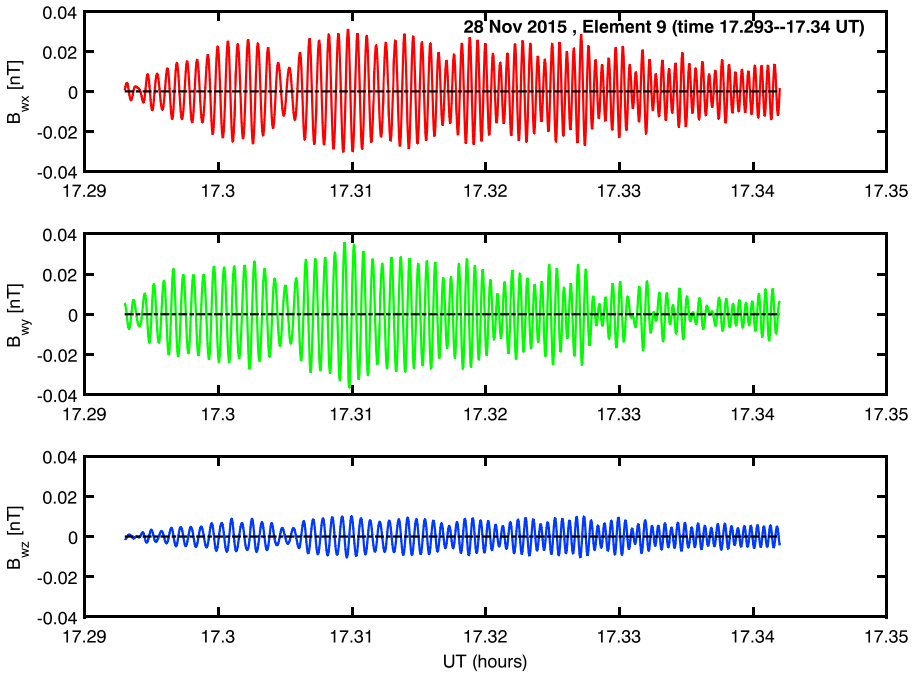

Figure 7. Filtered induction coil magnetometer data $\vec{B}_w = [B_{wx}, B_{wy}, B_{wz}]$ are shown as a function of time for element-9. Time duration of this element is 17.293–17.340 UT (hr) on 28 November 2015.

EMIC rising tone emission from event 1. This EMIC rising tone emission is element-9 (marked by an arrow in Figure 1a), and its duration is 17.293–17.340 UT (hr) on 28 November 2015. As mentioned in the previous section, we use the filtered ICM data in the present analysis (event 1). These filtered signals $\vec{B}_w = [B_{wx}, B_{wy}, B_{wz}]$ are shown in Figure 7 for element-9 of event 1. First, we identified the time of each zero crossing of a signal and the maximum amplitude of signal after each zero crossing. The reciprocal of the twice of the time difference between successive zero crossings represents the instantaneous frequency (i.e., $f^l_w = 1/2\Delta t$, where Δt is the time difference between successive zero crossing), and the peak absolute amplitude of a signal bounded by these successive zero crossings give the instantaneous amplitude. Thus, we estimated the instantaneous amplitude and frequency from B_{wx} and B_{wy} components and assigned their values to B^l_{wx}, B^l_{wy}, and f^l_{wx}, f^l_{wy}, respectively. It may be noted that the amplitude of B_{wz} is considerably small, compared to other two components (see Figure 7). As it is smaller, we have neglected its contribution while estimating the instantaneous amplitude. The instantaneous amplitude and frequency of EMIC wave is defined as $B^l_w = (B^l_{wx} + B^l_{wy})/2$ and $f^l_w = (f^l_{wx} + f^l_{wy})/2$. The time variations of instantaneous amplitude and frequency for element-9 are shown in Figures 8a and 8b respectively. Several peaks are noticed in the variation of instantaneous amplitude B^l_w (refer Figure 8a), which corresponds to subpacket structures present within one EMIC rising tone emission. The peak amplitude ($B^{subpacket}_{max}$) and duration ($T_D = t_2 - t_1$) of one such subpacket structure is marked by arrows in Figure 8a. Here 12–13 subpacket structures are clearly evident in original filtered signal and the variation of instantaneous amplitude. It is seen that the instantaneous frequency is increasing with time within this rising tone emission. A careful scrutiny of higher frequency (>0.5 Hz) portion of instantaneous amplitude-frequency plot shown in Figure 8 suggests that each peak in the amplitude is associated with a corresponding dip in the frequency. It means that the instantaneous frequency and amplitude are anticorrelated. In general, it is in agreement with nonlinear theory of EMIC wave (Shoji & Omura, 2013), which supports the inverse relation for wave amplitude and wave frequency when the maximum optimum amplitude is achieved. This tendency is evident in Figure 13, where we are comparing ground EMIC wave observations with nonlinear theory.

For each event, rather than looking at a single rising tone emission, we chose an interval of EMIC activity to execute the instantaneous amplitude-frequency analysis. This duration is marked with vertical dotted lines in Figure 1 for events 1–6. Time variations of instantaneous amplitude and frequency for event 1 during 17.05–17.7 UT are depicted in Figures 9a and 9b respectively. Overall, six rising tone EMIC emissions were present during this time interval, which is manifested as six peaks in the variation of instantaneous amplitude. After the triggering of EMIC wave rising tone, an increase in amplitude is found to be associated with an

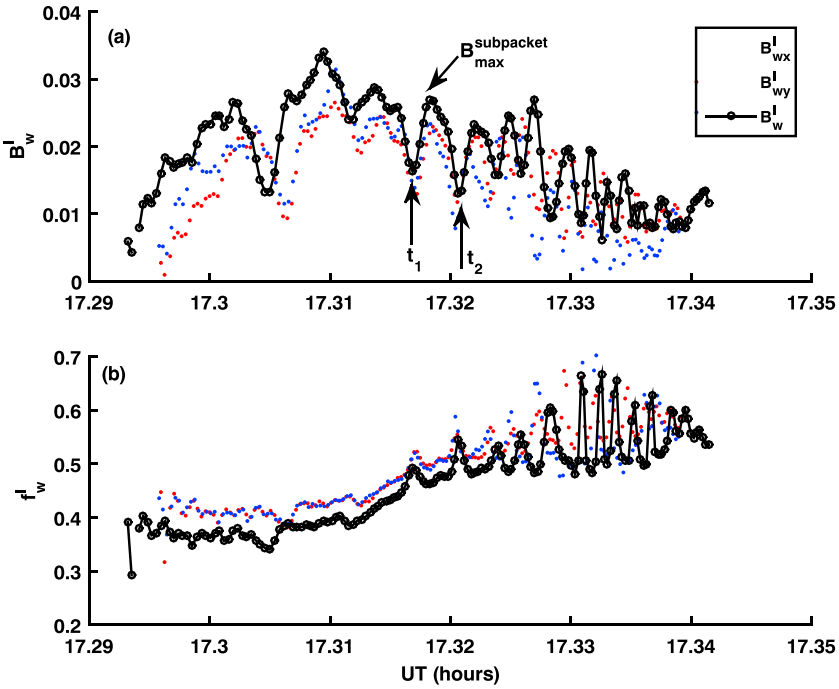

Figure 8. The time variation of (a) instantaneous amplitude B^l_w and (b) instantaneous frequency f^l_w for element-9 of event 1 are shown. The peak amplitude ($B^{subpacket}_{max}$) and duration ($T_D = t_2 - t_1$) of one subpacket structure is marked by arrows. Nearly 12–13 subpacket structures are clearly evident in the variation of instantaneous amplitude.

increase in frequency within the EMIC rising tone emissions. In order to verify the consistency of the behavior of the instantaneous amplitude and frequency, we carried out a similar analysis for all events. Figures 10a and 10b respectively shows the time variations of instantaneous amplitude and frequency for event 6, which is associated with helium band. It indicates that each EMIC rising tone emission consist of several subpacket structures. We find that for the proton band, that is, events 1–4 (helium band, i.e., 5–6) 6–12 (4–5) subpacket

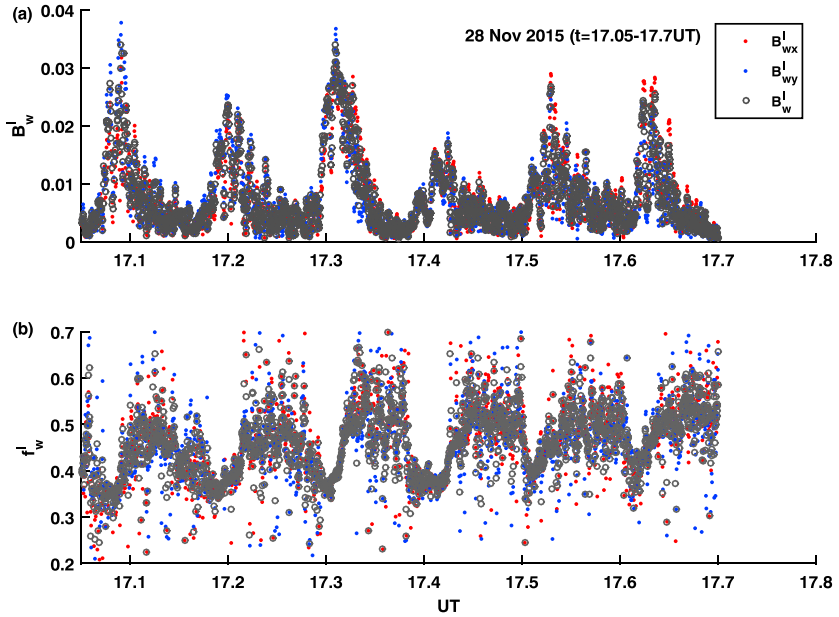

Figure 9. Time variation of instantaneous (a) amplitude and (b) frequency for event 1 (H-band) during 17.05–17.7 UT are depicted here.

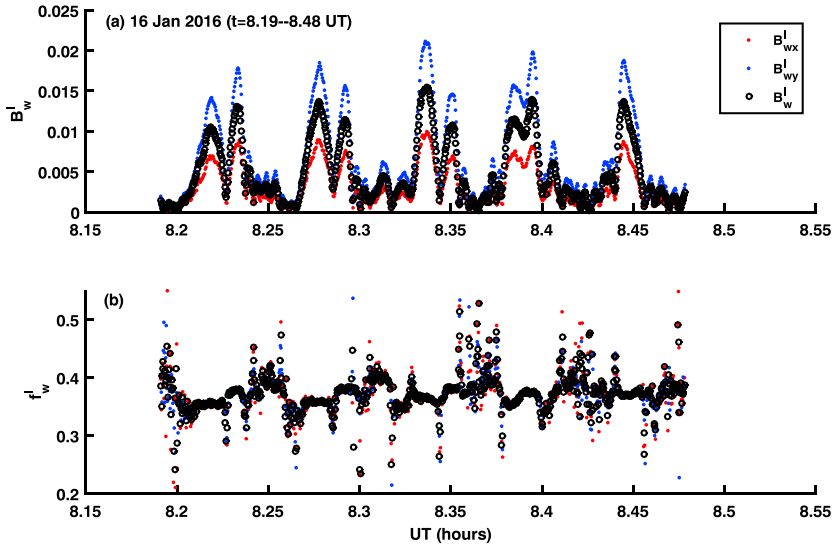

Figure 10. Time variation of instantaneous (a) amplitude and (b) frequency for event 6 (He-band) during 8.19–8.48 UT are depicted.

structures are associated with each rising tone EMIC emission. The presence of less number of subpacket structures for the helium band EMIC emission is attributed to its smaller frequency extent.

In addition, for each event, we have gathered information of strength of subpacket structure ($B^{subpacket}_{max}$) and its duration T_D. These estimates are obtained for the interval for which the instantaneous amplitude-frequency analysis is performed. In Figures 11a–11f the strength of the subpacket structure is plotted as a function of its duration for events 1–6. It is clearly evident that the strength of EMIC subpacket structures is controlled by the duration of the subpacket structure. The correlation coefficients between strength and duration of subpacket structures are in the range of 0.53–0.87 for events 1–6. This tendency is consistent and seen for all events studied here. This behavior can be understood based on the nonlinear wave growth rate Γ_{NL} given by Omura et al. (2010). The nonlinear wave theory suggests that the nonlinear growth rate of the wave is inversely proportional to the amplitude of wave, that is, $\Gamma_{NL} \propto 1/B_w$. Thus, the larger amplitude waves grow slowly and give rise to longer durations. This supports the observed tendency of association of longer duration of subpacket structures with larger amplitudes. Recently, such behavior is also seen in the chorus waves, where the amplitude of subpacket found to decrease with increase in frequency of subpacket (Santolík et al., 2014).

6. Comparison with the Nonlinear Theory

In this section, we compare instantaneous amplitudes and frequencies of the ground EMIC observations with the nonlinear wave theory (Omura et al., 2010). It is applicable to both proton and helium band EMIC waves. In the generation region, comparison of satellite observation of the EMIC waves with the theory is relatively easy as one can identify the EMIC bands based on the knowledge of local particle gyrofrequencies (qB_0/m_s, here s=H^+, He^+, O^+). However, identification of the EMIC bands from the ground observations is not straightforward. Thus, to compare these ground EMIC wave observations with the theory we need information of proton/helium gyrofrequencies. As discussed in section 3, based on the frequency extent, we speculate that the EMIC activities for events 1–4 (5–6) may be associated with proton (helium) band. Now we want the information on proton/helium gyrofrequency. Here we have assumed that the EMIC waves are propagating away from the source region along the magnetic field lines after their generation (Loto'Aniu et al., 2005). When these EMIC waves arrive at their footprints in the ionosphere, the wave signatures can be recorded by the ground nearby ICMs as well as by distant ICMs because of propagation effects in the ionospheric duct. However, EMIC wave power is likely to undergo attenuation during such propagation, and this attenuation is significant for higher frequencies of the EMIC wave (H. Kim et al., 2011). From ground observations, we estimated the upper frequency bound for EMIC wave, which is termed as f_u. This frequency is multiplied by a factor of 1.2 to compensate for the attenuation of higher frequencies of the EMIC wave. It means that the upper frequency bound for the observed EMIC wave can lie in the range of f_u–$1.2f_u$. By treating these upper bound frequencies as a proton (events 1–4) and helium (events 5–6) gyrofrequencies, we estimated the ambient magnetic field by

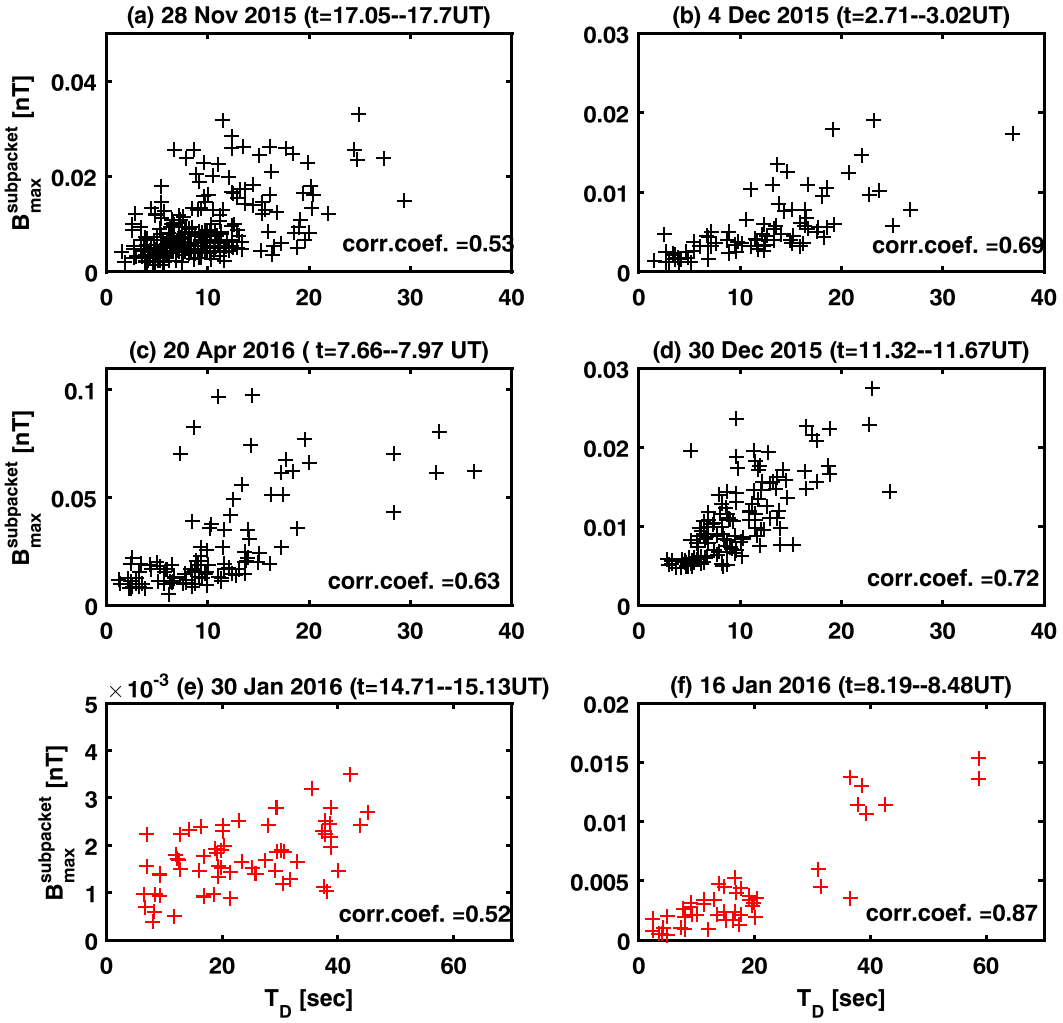

Figure 11. (a)–(f) Strength of subpacket structure ($B_{max}^{subpacket}$) is plotted as a function of its duration T_D for events 1–6.

using $B_0 = 2\pi f_u m_s/q$, where m_s is mass of proton or mass of helium depending on the corresponding frequency band. Thus, we have probable range of gyrofrequencies and the corresponding ambient magnetic field in the source region, which are given in Table 2.

All EMIC events studied here are associated with the magnetically quiet days. In such scenario, one can assume less modulation in the dipolar configuration of the Earth's magnetic field. We use the International

Table 2
Estimates of Gyrofrequencies (From the Observations), Ambient Magnetic Field (From the International Geomagnetic Reference Field Model), L-shell (from the International Geomagnetic Reference Field Model), and the Ambient Electron Density (From the Model) for the Events 1–6 are Summarized

Event no.	Day	$f_u - 1.2f_u$ (Hz)	$B_0 = 2\pi f_u m_s/q$ (nT)	L (R_E)	L_{pp} (R_E)	$n_{e0} \approx n_{i0}$ (/cc)	EMIC band
1	28 Nov 2015	0.66–0.79	43–52	8.2–8.7	6.5 ± 0.12	2.9–2.3	H-band
2	4 Dec 2015	0.71–0.85	47–56	8–8.5	7.7 ± 0.22	3–2.5	H-band
3	20 Apr 2016	0.79–0.95	52–62	7.7–8.2	5.4 ± 0.05	3.8–3	H-band
4	30 Dec 2015	0.64–0.77	42–51	8.3–8.8	7.0 ± 0.18	2.8–2.2	H-band
5	30 Jan 2016	0.29–0.35	76–91	6.8–7.2	6.6 ± 0.15	6.2–5	He-band
6	16 Jan 2016	0.48–0.58	126–151	5.7–6.1	7.0 ± 0.17	45–63	He-band

Note. EMIC = electromagnetic ion cyclotron.

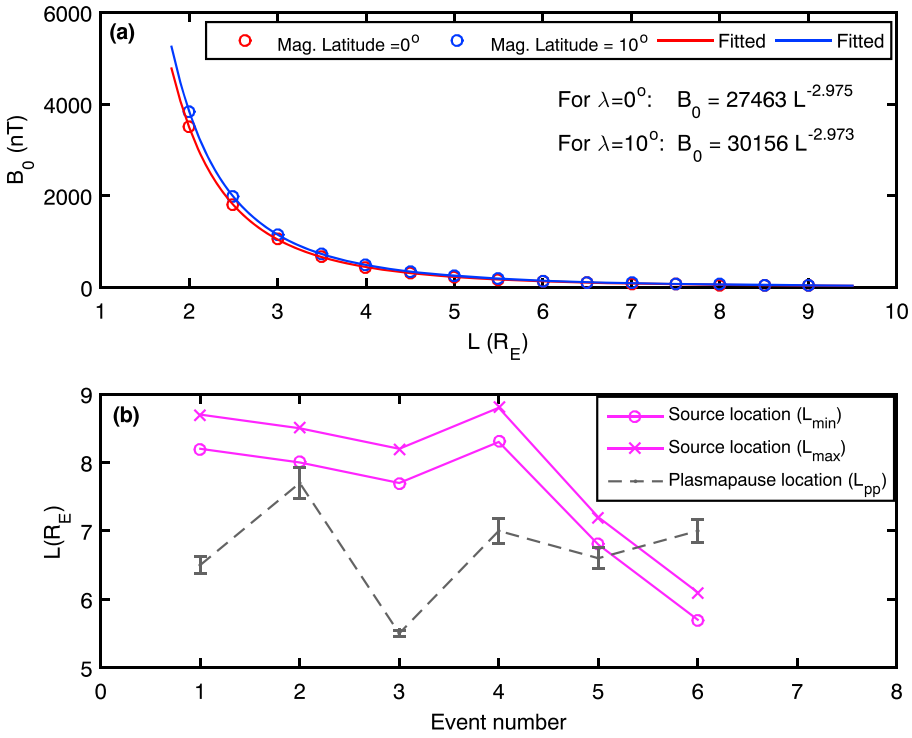

Figure 12. (a) The variation of B_0 as a function of *L*-shell derived from the International Geomagnetic Reference Field model is shown for magnetic latitude (λ) 0° and 10°N. (b) Model derived magnetopause location and *L*-shells of possible location of electromagnetic ion cyclotron wave source are shown for events 1–6.

Geomagnetic Reference Field model to obtain the ambient magnetic field for different values of the *L*-shell in the low latitude zone (source region) for a quiet day. The variation of B_0 as a function of *L*-shell is shown in Figure 12a for the magnetic latitude (λ) 0° and 10°. We find that the ambient magnetic field and *L*-shell are best manifested by B_0=27463L$^{-2.975}$ in the equatorial region. Here B_0 is expressed in nT and *L*-shell is expressed in the units of the Earth's radius R_E. Using this empirical relation, we computed the range of *L*-shell for all the EMIC events. These estimates are given in Table 2.

Further, we estimated the location of plasmapause (L_{pp}) using an empirical equation given by O'Brien and Moldwin (2003). The equation is $L_{pp} = a \times AE_{max} + b$, where $a = -2.86 \pm 0.11$, $b = 12.4 \pm 0.3$. This empirical equation requires the maximum value of high latitude geomagnetic activity index *AE* as an input. For each event we obtained the value of AE_{max} during the periods of EMIC waves that are mentioned in Table 1. The estimated values of plasmapause location are given in Table 2. Figure 12b shows the plasmapause location estimated from model and the possible *L*-shell of EMIC wave generation source in the equatorial region for events 1–6. It may be noted that for events 1–5 the possible source of EMIC wave is located outside the plasmapause (i.e., $L_{pp} < 7$). The next step is to get the ambient electron density at the EMIC wave source location. In the dipolar magnetic field configuration, one can obtain the ambient electron density using the following empirical relation (Sheeley et al., 2001).

Inside the plasmapause,

$$n_{e0} = 1390[3/L]^{4.83}, \tag{5}$$

and outside the plasmapause,

$$n_{e0} = 124[3/L]^4 + 36[3/L]^{3.5}\cos[(LT - 7.7(3/L)^2 - 12)\pi/12]. \tag{6}$$

By substituting the *L*-shell values in the equation above, the ambient electron densities are obtained, which are given in Table 2. As source locations for events 1–5 (event 6) lie outside (inside) the plasmapause, we used equation (6) (equation (5)) to get the estimates of the density. Under the quasi-neutrality condition the electron density and proton density are assumed to be the same, that is, $n_{eo} \approx n_{Ho}$.

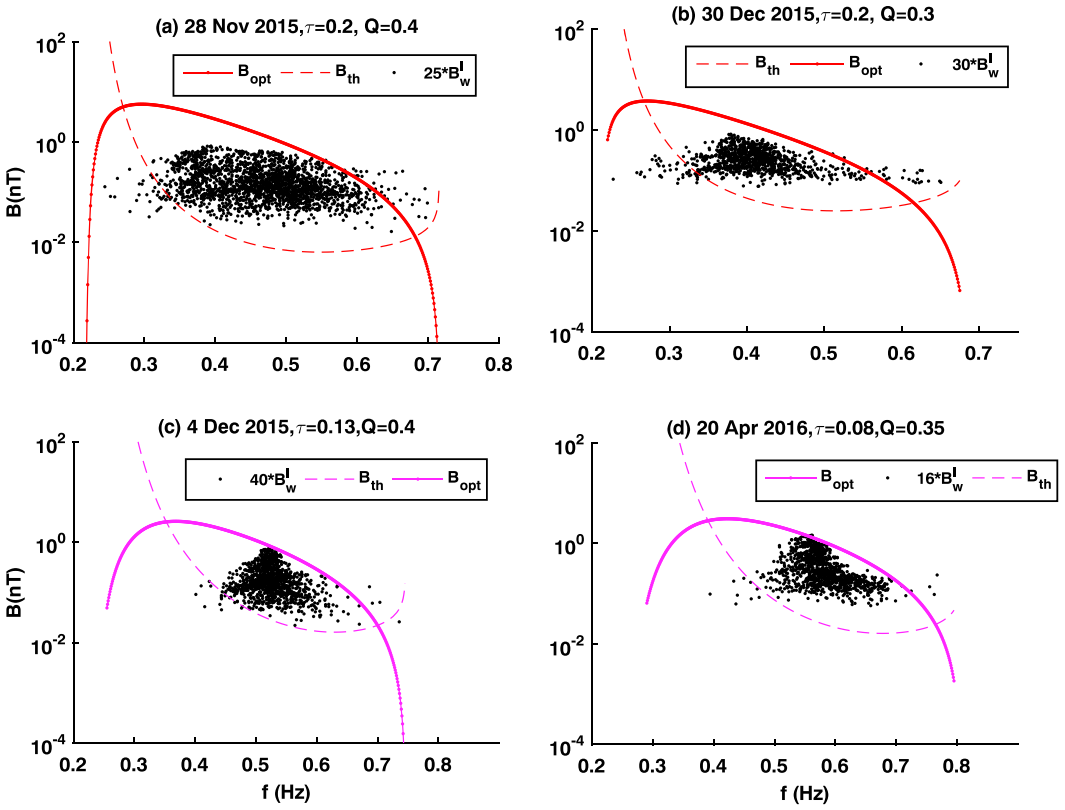

Figure 13. (a)–(d) Theoretical curves of optimum amplitude (B_{opt}) and threshold amplitude (B_{th}) superimposed with observed instantaneous amplitude are depicted as a function of frequency for events 1–4. The observed instantaneous amplitudes are multiplied by a factor in the range of 16–40 to compensate for the decrease in wave power due to attenuation during their propagation.

EMIC waves are generated by the ion cyclotron instability of energetic protons with an anisotropic temperature distribution with $T_\perp > T_\parallel$ and their generation is more likely in the low latitude region of the Earth's inner magnetosphere as the smaller magnetic field gradient in that region favors the generation of the EMIC wave. Omura et al. (2010) and Shoji and Omura (2013) have developed a nonlinear wave growth theory of EMIC triggered emissions observed in the inner magnetosphere. They have given the analytical expressions for the optimum (B_{opt}) and threshold (B_{th}) amplitudes of the EMIC rising tone emission. While the threshold amplitude represents the minimum amplitude of the constant frequency of the ion cyclotron wave required to trigger the EMIC wave, the optimum amplitude represents the maximum amplitude achievable by the EMIC wave through its nonlinear wave growth. From satellite observations, it has been shown that the observed amplitudes of EMIC subpacket structures are in good agreement with these theoretical estimates (Nakamura et al., 2015). Here we have estimated the threshold and optimum amplitudes of EMIC waves using the following equations.

$$B_{th} = \left(\frac{m_H}{q}\right)\Omega_{H0}^2 c^4 \left(\frac{as_2 V_{t\parallel}}{Q}\right)^2 \left(\frac{100\pi^3 V_P^3}{\omega\omega_{ph}^4 V_{\perp 0}^5}\right) \exp\left(\frac{V_R^2}{V_{t\parallel^2}}\right), \tag{7}$$

$$B_{opt} = \left(\frac{0.81\pi^{-5/2} m_H}{q}\right)\left(\frac{Q}{\tau}\right)\left(\frac{s_1 V_g}{s_0 \omega V_{t\parallel}}\right)\omega_{ph}^2 \left(\frac{V_{\perp 0}^2}{c^2}\right) \exp\left(\frac{V_R^2}{2V_{t\parallel}^2}\right). \tag{8}$$

In this theory the Earth's dipolar magnetic field is approximated by the parabolic equation described as $\Omega_H = \Omega_{H0}(1 + ah^2)$, where $a = 4.5/(LR_E)^2$, $\Omega_H = qB/m_H$ is the proton gyrofrequency at position h along magnetic field line, Ω_{H0} is the proton gyrofrequency at the magnetic equator, $\omega_{ph} = \sqrt{(n_h e^2/m_H \epsilon)}$ is the hot proton plasma frequency, and ω is the wave frequency. The parameters s_0, s_1, s_2 are given by

$$s_0 = V_{\perp 0}/V_P, \tag{9}$$

Table 3
Parameters Used to Obtain the Theoretical Estimates of Optimum and Threshold Amplitude of Electromagnetic Ion Cyclotron Wave are Summarized for all Six Events

Event no.	Day	n_{eo} (/cc)	$V_{\perp 0}/V_{t\|\|}$	$V_{t\|\|}$ (km/s)	$n_H : n_{He} : n_O$	n_h/n_H	B_0 (nT)	L (R_E)
1	28 Nov 2015	3.5	1.6	800	0.90:0.05:0.05	0.17	47	8.3
2	4 Dec 2015	3.5	1.4	500	0.90:0.05:0.05	0.11	49	8
3	20 Apr 2016	4.5	1.7	500	0.90:0.05:0.05	0.10	53	7.7
4	30 Dec 2015	3.0	1.6	900	0.90:0.05:0.05	0.13	45	8.4
5	30 Jan 2016	9	1.2	2,000	0.70:0.30:0	0.30	75	7
6	16 Jan 2016	50	1.1	1,400	0.75:0.25:0	0.18	126	6

$$s_1 = (1 - V_R/V_g)^2, \tag{10}$$

$$s_2 = \left(\frac{V_{\perp 0}^2}{2V_P^2} + \frac{V_R^2}{V_P V_g} - \frac{V_R^2}{2V_P^2}\right)\frac{\omega}{\Omega_H} - \frac{V_R}{V_P}, \tag{11}$$

where V_P and V_g are, respectively, the phase velocity and group velocity of the EMIC wave. The resonance velocity is given by $V_R = (\omega - \Omega_H)/k$. The nonlinear growth and optimum amplitude of the EMIC wave are controlled by the hot proton density n_H and hot proton temperature anisotropy, that is, $(V_{t\perp}/V_{t\|})^2$. The average velocity of the proton in the perpendicular direction is assumed to be equal to drift velocity of hot proton, that is, $\langle v_\perp \rangle = V_{\perp 0}$. Thus, the thermal velocity of protons in perpendicular direction becomes $V_{t\perp} = \sqrt{2/\pi}V_{\perp 0}$. Parameter Q is the depth of proton hole, and τ is a ratio of nonlinear transition time to trapping time of a resonant proton (Shoji & Omura, 2013).

A careful scrutiny of equations (7) and (8) yields the information of (i) L-shell; (ii) ambient magnetic field; (iii) ambient electron density n_{eo}; (iv) density of proton (n_H), helium (n_{He}), and oxygen (n_o); (v) hot proton density

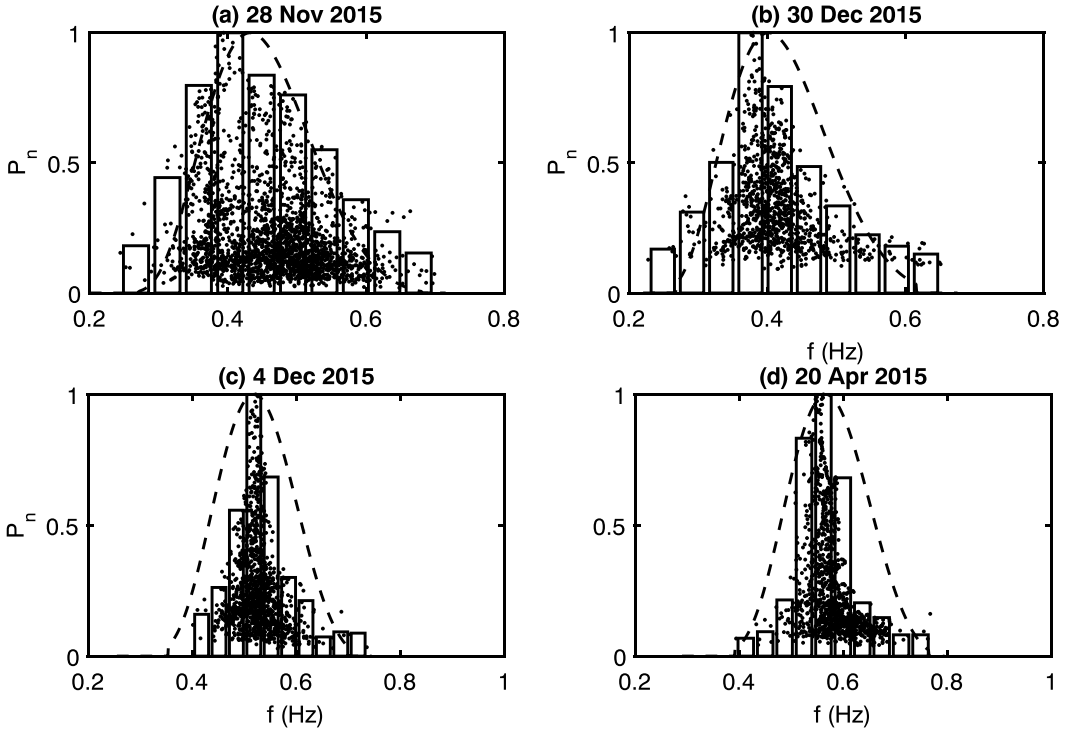

Figure 14. (a)–(d) The normalized distribution function P_n derived from the theory (dashed line) and observation (vertical bars with dots) as a function of frequency is plotted for events 1–4. It indicates that the probability distribution function associated with electromagnetic ion cyclotron ground observations are in good agreement with the theory.

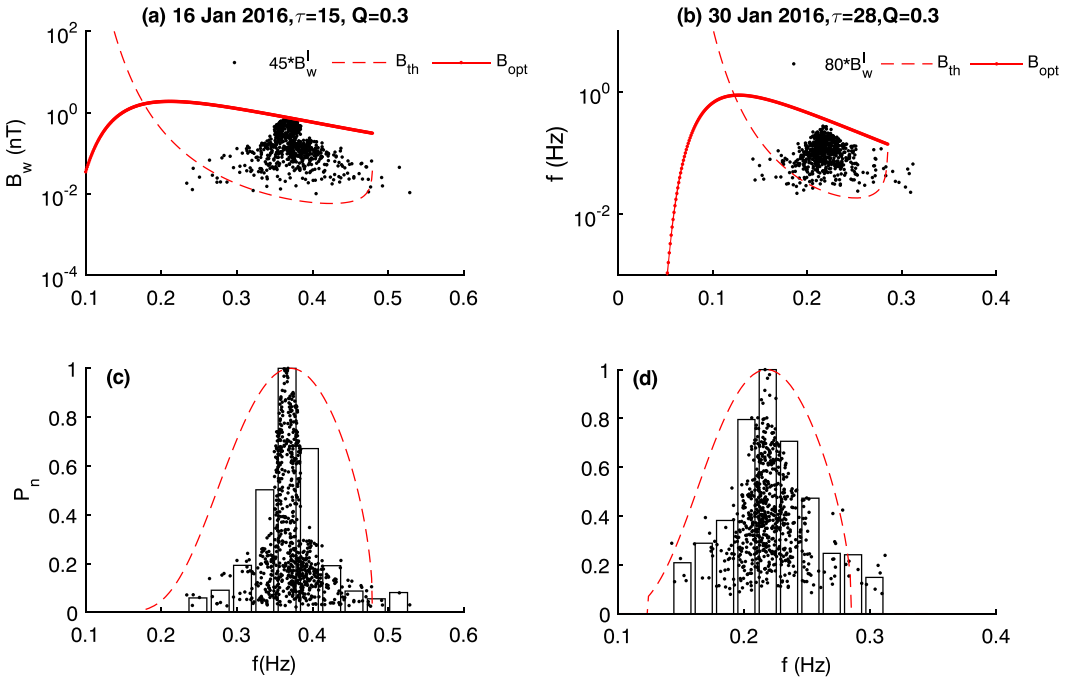

Figure 15. (a)–(b) Theoretical curves of optimum amplitude (B_{opt}) and threshold amplitude (B_{th}) superimposed with observed instantaneous amplitude are depicted as a function of frequency for events 5–6. The observed instantaneous amplitudes are multiplied by a factor in the range of 45–80 to compensate for the decrease in wave power due to attenuation during their propagation. (c)–(d) Normalized distribution functions P_n derived from theory (dashed line) and observation (vertical bars with dots) as functions of frequency are plotted for events 5–6.

n_h; and (vi) ratio of perpendicular to parallel thermal velocities of proton to estimate the threshold and optimum amplitudes of the EMIC wave. We obtained probable values of parameters mentioned in (i), (ii), and (iii) using observation and empirical models, which are summarized in Table 2. Typical values of the parameters (iv), (v), and (vi) are taken from Nakamura et al. (2015) as guess values. Further, we varied these parameters so that we can fit the estimates to the variation of instantaneous amplitude and frequency of the observed EMIC waves. Theoretical curves of the optimum and threshold amplitudes superimposed with the observed instantaneous amplitudes are depicted in Figures 13a–13d as functions of frequency for events 1–4. It may be noted that the observed instantaneous amplitudes are multiplied by factors in the range of 16–40 to compensate for the decrease in wave power due to attenuation through their propagation. The parameters used to get theoretical curves are mentioned in Table 3. It is seen that the amplitude-frequency relation of EMIC waves is in agreement with the threshold and optimum wave amplitudes given by the nonlinear theory.

Further, we carried out another exercise to test the tendency of the observed amplitude-frequency of the EMIC wave with the nonlinear theory. First, we estimated the ratio of the optimum amplitude to the threshold amplitude using the theory. For a given set of ambient parameters, this ratio $P = B_{opt}/B_{th}$ gives the probability of triggering of the EMIC wave in the frequency domain. Thus, the normalized probability distribution function is defined as $P_n = P/P_{max}$, which we compared with the observations. Now to obtain the probability distribution function from observations, we separated instantaneous frequency into 10 equal bins such that each frequency bin has a width of $\Delta f = (f_w^{l,max} - f_w^{l,min})/10$. For each chosen bin of frequency Δf, we estimated the average peak amplitude ($\langle B_w^l \rangle$) by picking first 10 values of maximum amplitude in that bin. The probability distribution of instantaneous amplitude in frequency domain is then obtained from normalized amplitude such that $P_n = \langle B_w^l \rangle / \langle B_w^l \rangle_{max}$. In Figures 14a–14d, we have plotted the normalized distribution functions P_n derived from the theory (dashed line) and observation (vertical bars with dots) as functions of frequency. For helium band EMIC, that is, events 5–6, we carried out a similar exercise and their results are presented in Figure 15. Figures 13, 14, and 15 indicate that the probability distribution functions associated with the EMIC ground observations are in good agreement with the theory. It witnesses the less propagational effect on the subpacket structure characteristics in the frequency domain. The ambient electron densities taken in the theoretical estimates are in the range of 3–50 /cc (i.e., ω_{pe} = 16–63 kHz) for L-shell of 6–8.3, which are comparable

to the model estimates of electron density listed in Table 2, that is, ω_{pe} = 13–71 kHz (Sheeley et al., 2001). An EMIC wave can undergo attenuation when (i) it is propagating along the magnetic field line away from the source region and (ii) during its propagation through ionospheric duct after its arrival at the footprint of the magnetic field line in the ionosphere. Among both, the later attenuation is significant and it is dependent on wave propagation direction, wave frequency, and ionospheric conditions. H. Kim et al. (2011) have reported that the attenuation is in the range of 10–14 dB per 1,000 km, which corresponds to $B_w^{source} = (3-5)B_w^{observed}$ per 1,000 km. In the dipolar configuration, the half length of the Earth's magnetic field line having foot prints on the ground at magnetic latitude 60°–70° is approximately 5–10 R_E. It means that the EMIC wave travels a distance of few tens of a thousands of kilometers along magnetic field line during its propagation to the ground. In the present study, we find that the observed instantaneous amplitude is 16–80 times smaller in magnitude as compared to the amplitudes estimated by the nonlinear theory for EMIC waves in the generation region. It may be noted that this attenuation factor is obtained by comparing ground EMIC observations with theoretical estimates of EMIC wave amplitudes in the generation region. However, one needs to explore the simultaneous conjugate EMIC wave observations from space and the ground for better understanding of the attenuation of EMIC waves during their propagation to the ground. For the events 1–6 we explored the possibility of simultaneous satellite (THEMIS, CLUSTER, RBSP) observations of EMIC waves but we could not find simultaneous satellite paths in the vicinity of source regions.

7. Summary and Conclusions

In this paper, we have studied the subpacket structure characteristics of EMIC waves in the ground magnetic records from the Indian Antarctic station Maitri. Six EMIC wave events occurred on magnetically quiet days of 2015–2016 are considered for the analysis. The signatures of rising tone EMIC waves are clearly evident in ground observations. Duration of EMIC events is around 1.4–2.5 hr. The occurrence of EMIC rising tone waves is found to be in the range of 1.9–6.7 min for these events, which are attributed to Pc5 ULF field line oscillations. More than 70% of times the EMIC events 1–5 are found to be associated with right-handed polarization, whereas the left-handed polarization is mainly seen for the event 6. The eccentricity and polarization analyses suggest that the EMIC waves observed on the ground are mainly characterized by right-handed elliptical polarization. Occasionally, left-handed elliptical polarization is also found to be present. Presences of subpacket structures are clearly evident in the ground EMIC observations. In the proton band, a single EMIC rising tone wave is associated with nearly 6–12 subpacket structures, whereas in helium band there are nearly 4–5 subpacket structures. The instantaneous amplitude-frequency analysis shows that the wave frequency increases during the period of increase in the amplitude of the EMIC rising tone wave. The duration of the subpackets is in the range of 2–60 s, and it is found to be dependent on the maximum amplitude of the subpacket structure. This tendency is consistent and found to be followed by all events studied here with the correlation coefficients of 0.53–0.87. Such tendency is followed by subpacket structures because the nonlinear growth rate is inversely proportional to the wave amplitude. Since a smaller amplitude subpacket has a higher nonlinear growth rate, its duration is shorter. The instantaneous amplitude-frequency information of subpacket structures retrieved from ground observations are compared with the theoretical estimates of the optimum and threshold amplitudes. The amplitude-frequency relation of the ground EMIC subpacket structures is found to be in good agreement with the theory. On the ground, the amplitude of the EMIC waves is found to be lower than the expected theoretical estimates of wave amplitude in the source region. This exercise reveals that the amplitude-frequency dependence of EMIC wave subpacket structures is not much affected during the propagation. In the frequency domain the EMIC wave information is not altered, while the amplitude is reduced by 16–80 times.

Acknowledgments

This study is carried out during visit of BK to RISH, Kyoto University, Japan. The study was supported by JSPS KAKENHI Grant 17H06140. We thank omniweb team for interplanetary data available at http://omniweb.gsfc.nasa.gov/ow_min.html, NASA NGDC team for IGRF model available at http://www.ngdc.noaa.gov/geomag-web, WDC Kyoto for AE index, and CDAWEB for location of satellites. We are thankful to R. Rawat for the technical support of the ICM experiment at Antarctica, Maitri. The ICM data will be made available on www.iigm.res.in on request at ashwini@iigs.iigm.res.in.

References

Carson, B. R., Rodger, C. J., & Clilverd, M. A. (2013). POES satellite observations of EMIC-wave driven relativistic electron precipitation during 1998–2010. *Journal of Geophysical Research: Space Physics*, *118*, 232–243. https://doi.org/10.1029/2012JA017998

Clilverd, M. A., Duthie, R., Hardman, R., Hendry, A. T., Rodger, C. J., Raita, T., et al. (2015). Electron precipitation from EMIC waves: A case study from 31 May 2013. *Journal of Geophysical Research: Space Physics*, *120*, 3618–3631. https://doi.org/10.1002/2015JA021090

Fraser, B., Grew, R., Morley, S., Green, J., Singer, H., Loto'aniu, T., & Thomsen, M. (2010). Storm time observations of electromagnetic ion cyclotron waves at geosynchronous orbit: GOES results. *Journal of Geophysical Research*, *115*, A05208. https://doi.org/10.1029/2009JA014516

Gendrin, R., Ashour-Abdalla, M., Omura, Y., & Quest, K. (1984). Linear analysis of ion cyclotron interaction in a multicomponent plasma. *Journal of Geophysical Research*, *89*(A10), 9119–9124.

Gomberoff, L., & Neira, R. (1983). Convective growth rate of ion cyclotron waves in a H+- He+ and H+- He+- O+ plasma. *Journal of Geophysical Research*, *88*(A3), 2170–2174.

Johnson, J. R., & Cheng, C. (1999). Can ion cyclotron waves propagate to the ground? *Geophysical research letters*, *26*(6), 671–674.
Jordanova, V., Albert, J., & Miyoshi, Y. (2008). Relativistic electron precipitation by EMIC waves from self-consistent global simulations. *Journal of Geophysical Research*, *113*, A00A10. https://doi.org/10.1029/2008JA013239
Kangas, J., Guglielmi, A., & Pokhotelov, O. (1998). Morphology and physics of short-period magnetic pulsations. *Space Science Reviews*, *83*(3-4), 435–512.
Kim, E.-H., & Johnson, J. R. (2016). Full-wave modeling of EMIC waves near the He+ gyrofrequency. *Geophysical Research Letters*, *43*, 13–21. https://doi.org/10.1002/2015GL066978
Kim, H., Lessard, M., Engebretson, M., & Lühr, H. (2010). Ducting characteristics of Pc 1 waves at high latitudes on the ground and in space. *Journal of Geophysical Research*, *115*, A09310. https://doi.org/10.1029/2010JA015323
Kim, H., Lessard, M., Engebretson, M., & Young, M. (2011). Statistical study of Pc1–2 wave propagation characteristics in the high-latitude ionospheric waveguide. *Journal of Geophysical Research*, *116*, A07227. https://doi.org/10.1029/2010JA016355
Kim, K.-H., Omura, Y., Jin, H., & Hwang, J. (2017). A case study of EMIC waves associated with sudden geosynchronous magnetic field changes. *Journal of Geophysical Research: Space Physics*, *122*, 3322–3341. https://doi.org/10.1002/2016JA023391
Kubota, Y., Omura, Y., & Summers, D. (2015). Relativistic electron precipitation induced by EMIC-triggered emissions in a dipole magnetosphere. *Journal of Geophysical Research: Space Physics*, *120*, 4384–4399. https://doi.org/10.1002/2015JA021017
Lorentzen, K., McCarthy, M., Parks, G., Foat, J., Millan, R., Smith, D., et al. (2000). Precipitation of relativistic electrons by interaction with electromagnetic ion cyclotron waves. *Journal of Geophysical Research*, *105*(A3), 5381–5389.
Loto'Aniu, T., Fraser, B. J., & Waters, C. L. (2005). Propagation of electromagnetic ion cyclotron wave energy in the magnetosphere. *Journal of Geophysical Research*, *110*, A07214. https://doi.org/10.1029/2004JA010816
Loto'Aniu, T., Fraser, B., & Waters, C. (2009). The modulation of electromagnetic ion cyclotron waves by Pc 5 ULF waves. *Annales Geophysicae: Atmospheres, Hydrospheres and Space Sciences*, *27*, 121–130.
Menk, F. W. (2011). *Magnetospheric ULF Waves: A Review* (pp. 223–256). Dordrecht: Springer Netherlands. https://doi.org/10.1007/978-94-007-0501-2_13
Meredith, N. P., Horne, R. B., Kersten, T., Fraser, B. J., & Grew, R. S. (2014). Global morphology and spectral properties of EMIC waves derived from CRRES observations. *Journal of Geophysical Research: Space Physics*, *119*, 5328–5342. https://doi.org/10.1002/2014JA020064
Meredith, N. P., Thorne, R. M., Horne, R. B., Summers, D., Fraser, B. J., & Anderson, R. R. (2003). Statistical analysis of relativistic electron energies for cyclotron resonance with EMIC waves observed on CRRES. *Journal of Geophysical Research*, *108*(A6), 1250–1264. https://doi.org/10.1029/2002JA009700
Millan, R., & Thorne, R. (2007). Review of radiation belt relativistic electron losses. *Journal of Atmospheric and Solar-Terrestrial Physics*, *69*(3), 362–377.
Min, K., Lee, J., Keika, K., & Li, W. (2012). Global distribution of EMIC waves derived from THEMIS observations. *Journal of Geophysical Research*, *117*, A05219. https://doi.org/10.1029/2012JA017515
Mourenas, D., Artemyev, A., Ma, Q., Agapitov, O., & Li, W. (2016). Fast dropouts of multi-meV electrons due to combined effects of EMIC and whistler mode waves. *Geophysical Research Letters*, *43*, 4155–4163. https://doi.org/10.1002/2016GL068921
Mursula, K., Braäysy, T., Niskala, K., & Russell, C. T. (2001). Pc1 pearls revisited: Structured electromagnetic ion cyclotron waves on polar satellite and on ground. *Journal of Geophysical Research*, *106*(A12), 29543–29553. https://doi.org/10.1029/2000JA003044
Nakamura, S., Omura, Y., & Angelopoulos, V. (2016). A statistical study of EMIC rising and falling tone emissions observed by THEMIS. *Journal of Geophysical Research: Space Physics*, *121*, 8374–8391. https://doi.org/10.1002/2016JA022353
Nakamura, S., Omura, Y., Shoji, M., Nosé, M., Summers, D., & Angelopoulos, V. (2015). Subpacket structures in EMIC rising tone emissions observed by the THEMIS probes. *Journal of Geophysical Research: Space Physics*, *120*, 7318–7330. https://doi.org/10.1002/2014JA020764
O'Brien, T., & Moldwin, M. (2003). Empirical plasmapause models from magnetic indices. *Geophysical Research Letters*, *30*(4), 1152. https://doi.org/10.1029/2002GL016007
Omura, Y., Pickett, J., Grison, B., Santolik, O., Dandouras, I., Engebretson, M., et al. (2010). Theory and observation of electromagnetic ion cyclotron triggered emissions in the magnetosphere. *Journal of Geophysical Research*, *115*, A07234. https://doi.org/10.1029/2010JA015300
Omura, Y., & Zhao, Q. (2013). Relativistic electron microbursts due to nonlinear pitch angle scattering by EMIC triggered emissions. *Journal of Geophysical Research: Space Physics*, *118*, 5008–5020. https://doi.org/10.1002/jgra.50477
Park, J.-S., Kim, K.-H., Shiokawa, K., Lee, D.-H., Lee, E., Kwon, H.-J., et al. (2016). EMIC waves observed at geosynchronous orbit under quiet geomagnetic conditions ($kp \leq 1$). *Journal of Geophysical Research: Space Physics*, *121*, 1377–1390. https://doi.org/10.1002/2015JA021968
Park, J.-S., Shue, J.-H., & Kim, K.-H. (2017). Dependence of electromagnetic ion cyclotron wave occurrence on north-south orientation of interplanetary magnetic field: THEMIS observations. *Journal of Geophysical Research: Space Physics*, *122*, 11354–11372. https://doi.org/10.1002/2017ja024507
Pickett, J., Grison, B., Omura, Y., Engebretson, M., Dandouras, I., Masson, A., et al. (2010). Cluster observations of EMIC triggered emissions in association with Pc1 waves near Earth's plasmapause. *Geophysical Research Letters,37*, L09104. https://doi.org/10.1029/2010GL042648
Pikkarainen, T., Kangas, J., Kiselev, B., Maltseva, N., Rakhmatulin, R., & Solovjev, S. (1983). Type IPDP magnetic pulsations and the development of their sources. *Journal of Geophysical Research*, *88*(A8), 6204–6212.
Rasinkangas, R., & Mursula, K. (1998). Modulation of magnetospheric EMIC waves by Pc 3 pulsations of upstream origin. *Geophysical Research Letters*, *25*(6), 869–872. https://doi.org/10.1029/98GL50415
Remya, B., Tsurutani, B. T., Reddy, R. V., Lakhina, G. S., & Hajra, R. (2015). Electromagnetic cyclotron waves in the dayside subsolar outer magnetosphere generated by enhanced solar wind pressure: EMIC wave coherency. *Journal of Geophysical Research: Space Physics*, *120*, 7536–7551. https://doi.org/10.1002/2015JA021327
Rodger, C. J., Raita, T., Clilverd, M. A., Seppälä, A., Dietrich, S., Thomson, N. R., & Ulich, T. (2008). Observations of relativistic electron precipitation from the radiation belts driven by EMIC waves. *Geophysical Research Letters*, *35*, L16106. https://doi.org/10.1029/2008GL034804
Saikin, A., Zhang, J.-C., Allen, R., Smith, C., Kistler, L., Spence, H., et al. (2015). The occurrence and wave properties of H+-, He+-, and O+-band EMIC waves observed by the Van Allen Probes. *Journal of Geophysical Research: Space Physics*, *120*, 7477–7492. https://doi.org/10.1002/2015JA021358
Santolík, O., Kletzing, C., Kurth, W., Hospodarsky, G., & Bounds, S. (2014). Fine structure of large-amplitude chorus wave packets. *Geophysical Research Letters*, *41*, 293–299. https://doi.org/10.1002/2013GL058889
Sheeley, B., Moldwin, M., Rassoul, H., & Anderson, R. (2001). An empirical plasmasphere and trough density model: CRRES observations. *Journal of Geophysical Research*, *106*(A11), 25631–25641.
Shoji, M., & Omura, Y. (2013). Triggering process of electromagnetic ion cyclotron rising tone emissions in the inner magnetosphere. *Journal of Geophysical Research: Space Physics*, *118*, 5553–5561. https://doi.org/10.1002/jgra.50523

Shoji, M., Omura, Y., Grison, B., Pickett, J., Dandouras, I., & Engebretson, M. (2011). Electromagnetic ion cyclotron waves in the helium branch induced by multiple electromagnetic ion cyclotron triggered emissions. *Geophysical Research Letters*, *38*, L17102. https://doi.org/10.1029/2011GL048427

Summers, D., Ni, B., & Meredith, N. P. (2007). Timescales for radiation belt electron acceleration and loss due to resonant wave-particle interactions: 2. Evaluation for VLF chorus, ELF hiss, and electromagnetic ion cyclotron waves. *Journal of Geophysical Research*, *112*, 1–21. https://doi.org/10.1029/2006JA011993

Summers, D., & Thorne, R. M. (2003). Relativistic electron pitch-angle scattering by electromagnetic ion cyclotron waves during geomagnetic storms. *Journal of Geophysical Research*, *108*(A4), 1143. https://doi.org/10.1029/2002JA009489

Usanova, M., Drozdov, A., Orlova, K., Mann, I., Shprits, Y., Robertson, M., et al. (2014). Effect of EMIC waves on relativistic and ultrarelativistic electron populations: Ground-based and Van Allen Probes observations. *Geophysical Research Letters*, *41*, 1375–1381. https://doi.org/10.1002/2013GL059024

Usanova, M. E., Mann, I. R., Kale, Z. C., Rae, I. J., Sydora, R. D., Sandanger, M., et al. (2010). Conjugate ground and multisatellite observations of compression-related EMIC Pc1 waves and associated proton precipitation. *Journal of Geophysical Research*, *115*, A07208. https://doi.org/10.1029/2009JA014935

Wang, D., Yuan, Z., Yu, X., Deng, X., Zhou, M., Huang, S., et al. (2015). Statistical characteristics of EMIC waves: Van Allen Probe observations. *Journal of Geophysical Research: Space Physics*, *120*, 4400–4408. https://doi.org/10.1002/2015JA021089

Yahnina, T., Yahnin, A., Kangas, J., Manninen, J., Evans, D., Demekhov, A., et al. (2003). Energetic particle counterparts for geomagnetic pulsations of Pc1 and IPDP types. *Annales Geophysicae*, *21*, 2281–2292.

Young, D., Perraut, S., Roux, A., Villedary, C., Gendrin, R., Korth, A., et al. (1981). Wave-particle interactions near $\Omega_H e+$ observed on GOES 1 and 2 1. Propagation of ion cyclotron waves in He+-rich plasma. *Journal of Geophysical Research*, *86*(A8), 6755–6772.

Yu, X., Yuan, Z., Wang, D., Li, H., Huang, S., Wang, Z., et al. (2015). In situ observations of EMIC waves in O+ band by the Van Allen Probe A. *Geophysical Research Letters*, *42*, 1312–1317. https://doi.org/10.1002/2015GL063250

Zhang, X.-J., Mourenas, D., Artemyev, A., Angelopoulos, V., & Thorne, R. (2017). Contemporaneous EMIC and whistler mode waves: Observations and consequences for MeV electron loss. *Geophysical Research Letters*, *44*, 8113–8121. https://doi.org/10.1002/2017GL073886